ARTICLE

Check for updates

A magnetically actuated dynamic labyrinthine transmissive ultrasonic metamaterial

Christabel Choi [1]✉, Shubhi Bansal [1], James Hardwick[1], Niko Münzenrieder[1,2], Manish K. Tiwari [3,4] & Sriram Subramanian [1]

Currently, space-coiling acoustic metamaterials are static, requiring manual reconfiguration for sound-field modulation. Here, we introduce an approach to enable active reconfiguration, using standalone dynamic space-coiling unit cells called dynamic meta-bricks. Unlike their static counterparts, these meta-bricks, house an actuatable soft robotic-inspired magnetorheological elastomeric flap. This flap operates like a switch to directly control the transmitted ultrasound. For scalability, we present a hybrid stacking method, which vertically combines static and dynamic meta-bricks. This allows us to form a surface-integrated metasurface through concatenating variations of either fully static or hybrid stacks. By actuating dynamic metasurface sections, we experimentally demonstrate accurate modulation of $\lambda/4$ (≈ 2 mm) between two acoustic twin traps. We shift a levitated bead between the traps, validating that full-array operational dynamicity is achievable with partial, localised actuation. This work showcases the synergy between active and passive reconfigurability, opening possibilities to develop multifunctional metamaterials with additional degrees of freedom in design and control.

[1] Department of Computer Science, Faculty of Engineering, University College London, London WC1E 6BT, UK. [2] Faculty of Engineering, Free University of Bozen-Bolzano, Bozen 39100, Italy. [3] Wellcome/EPSRC Centre for Interventional and Surgical Sciences, UCL, London W1W 7TS, UK. [4] Nanoengineered Systems Laboratory, Mechanical Engineering, UCL, London WC1E 7JE, UK. ✉email: christabel.choi.19@ucl.ac.uk

In the current age of smart materials, acoustic metamaterial (AMM) research has emerged at the forefront of innovation for sound manipulation technologies. Recently, schemes for reconfiguration have been keenly explored in AMMs to enhance complex wave shaping applications like acoustic levitation[1], cloaking[2,3], beam steering[4,5], and holographic imaging[6–8]. The ability to strategically control the physical shape or composition of a structure on-demand is advantageous, as it allows greater functional flexibility and deployment efficiency. Real-time operation is achieved when the sound field is modulated upon actuation. This means that an assembled AMM need not be reassembled to generate a different sound field. Real-time control with active[9] designs has been reported using piezoelectric[10–14], magnetic[15,16], and electromagnetic[17–19] actuation, but most designs have been limited to sound attenuation applications. In this work, by using a transmissive AMM as a platform, we demonstrate an approach to exploit the synergy between active and passive reconfigurability methods for "dynamic sound modulation". "Sound modulation" implies that the input waves are modulated through the AMM to give a modified output. This output is fixed. "Dynamic sound modulation" means that the previously fixed output can be changed on-demand to a different, separate output, given the same input. This modulation is carried out using the same device (i.e., same unit cell, or set of unit cells), and is also done in real-time. A combination of active and passive reconfigurability methods allows greater degrees of freedom in design and control, through the expansion of available design parameters such as actuation state, or the arrangement of unit cells within a metasurface (i.e., a two-dimensional AMM[20]).

For transmissive applications, space-coiling[21–26] AMMs are ideal because of their high energy transmission, a wide scope for amplitude and phase modulation, adaptability over a large bandwidth, and non-resonant dispersion[27,28]. Sound travels through labyrinthine space-coiling geometries for a modified phase output, where the phase change is a function of a specific time delay. However, to date, these space-coiling AMMs are still conventionally passive. Manual reconfiguration of these metasurfaces has only been demonstrated through modular assembly of metamaterial unit cells, where each unit cell has a specific labyrinthine geometry, and hence a unique phase difference. This means that space-coiling metasurfaces must always be reassembled to produce a different output sound field. To the best of the authors' knowledge, there has been no previous attempt for active reconfiguration of space-coiling unit cells. Here, we introduce a transmissive dynamic space-coiling assembly metamaterial unit cell which allows in-situ active reconfigurability within an otherwise static metamaterial. Hence, a user-defined ultrasonic (>20 kHz) sound field can be manipulated on-demand without the need for reassembly.

Our unit cell is a dynamic version of a space-coiling static metamaterial brick (shortened to "meta-brick")[4], called a dynamic meta-brick. Static meta-bricks only have a single, fixed acoustic wave output. Dynamic meta-bricks can produce two acoustic wave outputs using a binary tunable propagation path, making them more versatile than their static counterpart. One of the challenges in designing and fabricating the dynamic meta-brick is the need for an internal actuation response mechanism. For airborne ultrasonic operation at 40 kHz, the components are at subwavelength dimensions (less than $\lambda = 8.66$ mm) on the millimetre scale. Therefore, the mechanism must comply with these dimensions, and be fabricated/assembled internally within the meta-brick.

In the field of soft robotics[29–31], active reconfiguration of surface structures has been made possible using magnetorheological elastomers (MRE)[32]. Examples include movable external microplates that mimic the skin of a chameleon[33] or miniature robots that can form complex programmable time-varying shapes[34–36]. Such reported setups often operate within relatively open spaces or surfaces, especially for motions like stretching (e.g., sensors, electronic skins), travelling, or propulsion. In the AMM field, common magnetoactive designs use resonant membranes[15,37], for applications such as sound absorption or attenuation. Other MRE-based AMM designs have demonstrated buckling of a 3D lattice[38], or deformation of open-ended Mie resonator pillars[39] to control transmission. Until now, MRE structures have never been applied within space-coiling metamaterial unit cells for acoustic modulation. Structurally, space-coiling transmissive metasurfaces are compact and consist of repeating labyrinthine unit cells. These unit cell (and metasurface) geometries are spatially inaccessible, especially at ultrasonic frequencies (e.g., millimetre scale dimensions). However, we overcame these dimensional constraints to demonstrate that active MRE structures can be anchored within narrow, inaccessible spaces like meta-bricks.

Our method for tunability employs magnetic actuation of a planar rectangular MRE flap to create a controllable internal cantilever-like mechanism within the enclosed labyrinthine channel of the dynamic meta-brick. By harnessing the elastic mobility and magnetic responsivity characteristics of MRE materials, we enable rapid and robust transitions in the ultrasound propagation path. The subwavelength MRE flap has similar dimensions (i.e., thickness, width) to the static flaps which are found within the original static meta-bricks. Our setup utilises a film-based assembly technique to incorporate the millimetre-scale MRE flap for binary acoustic switching. The proposed manufacturing method offers a versatile, low-cost, and accessible way to modify internal surfaces and secure elements within narrow apertures without disturbing the structure's exterior.

In this work, we demonstrate that a metasurface does not have to be fully dynamic to generate a dynamic output. In conventional methods, an active metasurface is formed from a full array of actively controllable unit cells[17,40], similar to the operation of phased array transducers (PAT) which are expensive, and currently involve a high degree of electronic and computational complexity[41–43]. Certain unit cells may be deactivated during operation, however they are not passive structures, and still part of a fully active system. Here, we combine fabricated static and dynamic meta-bricks together through stacking (where meta-bricks are vertically placed on top of each other), using a constrained phase retrieval algorithm to create a composite stacked metasurface. Hybrid meta-brick stacks (where both the static and dynamic meta-bricks are stacked together) within the metasurface allow a greater variety in distinct sets of binary phase values, as originally static meta-bricks can be rendered "dynamic" on-demand.

We confine the dynamic meta-bricks to the edges of the metasurface. By magnetically controlling the edge bricks, the metasurface permits accurate sound modulation on the millimetre-scale between two acoustic twin traps by a distance of $\lambda/4 \approx 2$ mm, shown through simulations and experiments. To assess the validity and speed of the real-time modulation of the sound field, we tweeze a lightweight bead (Fig. 1a) within the twin traps in mid-air. To date, acoustic levitation with transmissive metamaterials has only been static. Targeted, spatial ultrasound modulation in real-time has implications for different application domains like energy harvesting, haptics and virtual reality/augmented reality[44,45]. For instance, in commercial audio applications (e.g., audio spotlight® by Holosonics Research Labs, Inc.), the use of metamaterials could potentially allow a narrow beam of sound to be directed dynamically to specific locations on-demand.
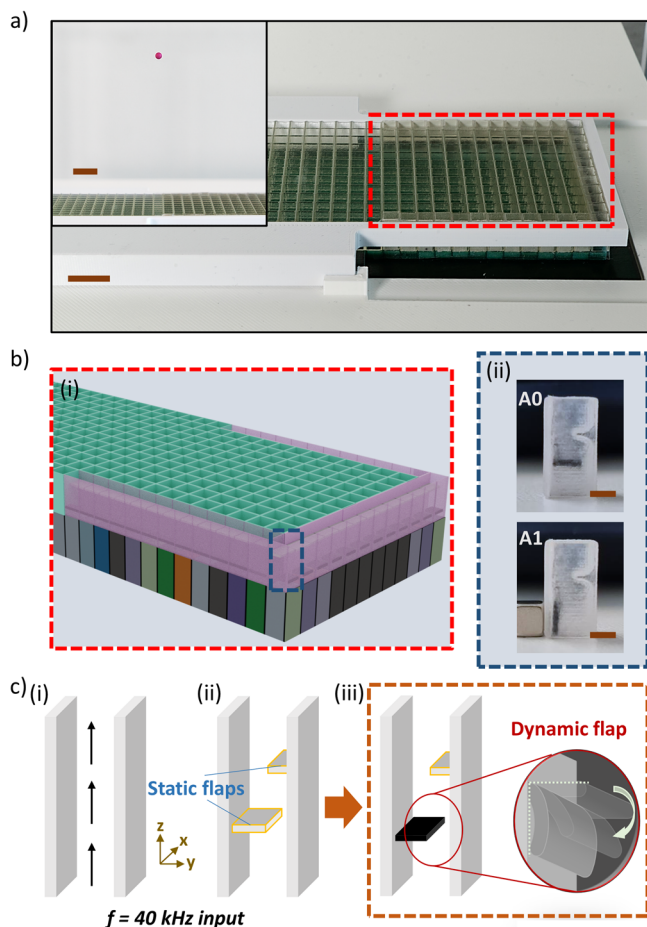
Fig. 1 Design and operation of dynamic meta-bricks, showing the concept of in-situ reconfigurability within an assembled metamaterial array.
a Photograph of metasurface, showing acoustic levitation of a pink polystyrene bead in the inset. Scale bars, 1 cm. **b** (i) Schematic of multi-layered metasurface, showing section within dashed red box in (**a**). (ii) Photograph of unactuated meta-brick (A0) and actuated meta-brick (A1) states, showing the meta-brick highlighted within the dashed blue box in (i). Scale bars, 2 mm. **c** Schematics of the cross-section of three meta-bricks. (i) The first meta-brick does not have any flaps. The black arrows represent the direction of propagation, with a 40 kHz input from below. (ii) The second meta-brick shows how the static flaps (outlined in yellow) form maze-like obstacles within the channel to increase the general path length for the travelling soundwaves. (iii) For the third meta-brick in the dashed orange box, the bottom flap is replaced by a black dynamic flap. Within the inset, it shows that the dynamic flap can move downwards in the direction of the arrow within the 90-degree range encompassed by the dotted lines.

This proof-of-concept showcases how the inclusion of a defined set of dynamic metamaterial unit cells can enhance deployment efficiency and enable greater dynamicity within reconfigurable metamaterials. By strategically utilising the interplay between active and passive components, this work therefore demonstrates a paradigm for engineering versatile, tunable, multifunctional next-generation metamaterials.

Results

Design and concept of dynamic meta-brick. Figure 1c illustrates how the presence of internal protuberances from the sidewalls, called flaps (with a minimum number of two), in a meta-brick can create a labyrinthine (space-coiling) path for the soundwaves to travel through. Meta-bricks can be scaled to work at lower frequencies (e.g., audible regime < 20 kHz)[46], but here, these flaps

are designed for 40 kHz airborne ultrasonic operation, with subwavelength dimensions (less than $\lambda = 8.66$ mm). 40 kHz ultrasound is useful for applications such as contactless manipulation and haptic feedback[41,47]. In traditional space-coiling structures, these flaps are static and do not move. The path length of each meta-brick is fixed due to their specific geometry, placement of the flaps, as well as the dimensions of the walls. To alter the path length within each unit cell, the geometry or position of one or a combination of internal components, i.e., sidewalls, or flaps, must change. As the flat internal faces of the sidewalls are difficult to modify during operation, the proposed dynamic component we modified was a flap.

To demonstrate a controllable path length for the meta-bricks, the mechanism we used to deploy the dynamic component (flap) was a bi-stable structure. The default state at rest gives a certain stable output, and the actuated state gives another stable output. To enable this bi-stable system, the type of actuation for the dynamic flap was chosen to be magnetic field actuation. This was determined by two main factors: (1) the range and plane of movement of the flap, and (2) the physical constraints of the surrounding passive structures, e.g., other flaps. While attached on one end of the flap to the wall near the base of the meta-brick, the range of movement for the dynamic flap was constrained only for downwards movement during actuation with rotation about the x-axis within a maximum range of 90 degrees, as shown in Fig. 1. This downward movement of the longer dynamic flap was enforced to prevent any obstruction of the static flap positioned higher up along the opposing meta-brick wall.

There are common actuation methods for cantilever-type structures, but appropriate actuation for the application depends on the mechanical characteristics of the cantilever. If the cantilever is completely rigid, the tethered end would require a hinge to enable flapping movements. The meta-brick walls are thin with a thickness of 0.5 mm or less, which makes it highly challenging to integrate a hinge mechanism for the dynamic flap and to implement mechanical actuation with motors. The same fabrication limitation applies to pneumatic or microfluidic actuation, which involves channel integration. For a less rigid cantilever which allows deflection, a hinge mechanism is not required. An electrostatic approach is commonly considered to actuate hinge-less microelectromechanical systems (MEMS) cantilevers[48,49] and membranes[50] with nano- or micro-scale thicknesses. While this could be a viable actuation method for very thin structures, it may not be suitable for a hinge-less meta-brick flap with millimetre-scale dimensions. Relative to MEMS cantilevers, our flap would be considered very thick, and would have difficulty achieving a high deflection angle without a mechanical hinge. Alternatively, if the dynamic flap was reduced to MEMS-scale dimensions, it would be too small compared to the operating wavelength to effectively modulate sound at 40 kHz. In addition, we must consider that our meta-brick is a transmissive AMM, which cannot be obstructed at the input and output, i.e., above and below the meta-brick. The sound source is positioned vertically below the meta-brick, and waves propagate through the brick to emerge from the top.

Hence, we overcame the aforementioned limitations by an actuation method inspired by soft robotics (millimetre-scale) – magnetic actuation. Within a magnetic field, the dynamic flap is able to respond and move within the meta-brick. Even if the external magnetic field was produced by a magnet in close proximity to the device, it did not need to be positioned directly in the line of wave propagation, but along the exterior side wall with minimal obstruction. Using an MRE material for the dynamic flap eliminated the need for conventional hinge-like mechanisms which are challenging to fabricate on a small scale, and tend to experience high amounts of friction during rotation.

Thus, we were able to achieve the maximum deflection angle (90 degrees) for our meta-brick. Silicone elastomeric rubber is characterised by softness, flexibility, and elasticity, which also allowed the dynamic flap to move reversibly without the need for reset signals.

The MRE flap was attached to the internal face of a single side wall in the dynamic meta-brick, also denoted brick A '('Active'). As shown in Fig. 1b, the dynamic meta-brick can switch between two positions, i.e., straight (unactuated, state A0), and down (actuated, state A1). Figure 1c illustrates the composition of the dynamic meta-brick with a combination of a static and dynamic flap. Like the meta-brick with fully static flaps at the centre of the schematic, the flaps within the dynamic meta-brick form maze-like obstacles within the propagation channel for the soundwaves. As compared to the meta-brick without any flaps on the left, the soundwaves take a longer time to travel through the meta-brick due to an elongation of the path length[26], resulting in a time delay and phase shift. Hence, the active binary switching of the flap translates into a modifiable labyrinthine path in the meta-brick, to modulate the impinging acoustic wave in real-time.

Manufacture of dynamic meta-brick. The dynamic meta-brick comprises external and internal components. External components refer to the meta-brick shell (surrounding walls), and internal components refer to the static and dynamic flaps of different lengths. (see Supplementary Fig. 1, Supplementary Information for dimensions) The meta-brick shell along with the static flap, and the dynamic flap were fabricated using three-dimensional (3D) printing and moulding[51] techniques, respectively. (see Methods).

Our moulding method incorporated the use of planar glass plates. To fabricate the flaps, synthetic magnetite nanoparticles (0.2 μm in diameter) were mixed with Ecoflex™ 00-30 in a 1:3 ratio. This magnetic mixture was then cast within the 3D-printed moulds. As shown in Fig. 2, after dispensing, two glass plates were positioned on top of the mould to apply pressure downwards at the interface (purple arrows) with the uncured magnetic silicone. During the curing process, the moulds were also placed over a magnet which helped to keep the mixture stable within the mould. These steps reduced the curvature at the surface of the flap due to surface tension and ensured that when the process is repeated, there are minimal variations in the thickness of each flap. Any residue on the edges was then removed with a knife after curing. (see Supplementary Fig. 3 and Supplementary Note 1, Supplementary Information).

The 3D-printed moulds used in the fabrication were treated with a low-cost and accessible post-processing method we developed to prevent curing inhibition for the silicone curing step. Using a combination of washing and soaking at an elevated temperature, we removed polar, non-polar, and heat labile polymerisation inhibitors. (see Methods) Without microfabrication methods (e.g., spin-coating)[30], each flap was moulded with a consistent thickness of approximately 0.44 mm (consistent with static meta-brick flaps which are λ/20[4]), with a coefficient of variation (CV) of 1.3%. (see Supplementary Fig. 2, Supplementary Information).

To assemble the dynamic meta-brick, we used an external film-based assembly technique (Fig. 2). The requirement to position the flap deep within the meta-brick eliminated the feasibility of using tweezers for accurate insertion. Due to its petite and slender structure, splitting and printing the meta-brick as separate components could lead to warping or brittleness. Consequently, we printed the meta-brick's shell in one piece. Afterward, the flap was affixed externally to a strip of Polyethylene terephthalate (PET, 100 μm thick and 3.5 mm wide) using Loctite precision liquid super glue (see Supplementary Note 1). Note that the strips were longer than the length of the meta-brick to make them easier to handle. Thereafter, the strips, with the flaps glued to them, were adhered to the side wall using gel super glue (Scotch® Super Glue Liquid). The last step was to cut away the excess edges of the PET strip. Within the meta-brick, there was a clearance of around 0.25 mm between the flap edges and the internal meta-brick walls to prevent friction during actuation. (see Supplementary Fig. 1,
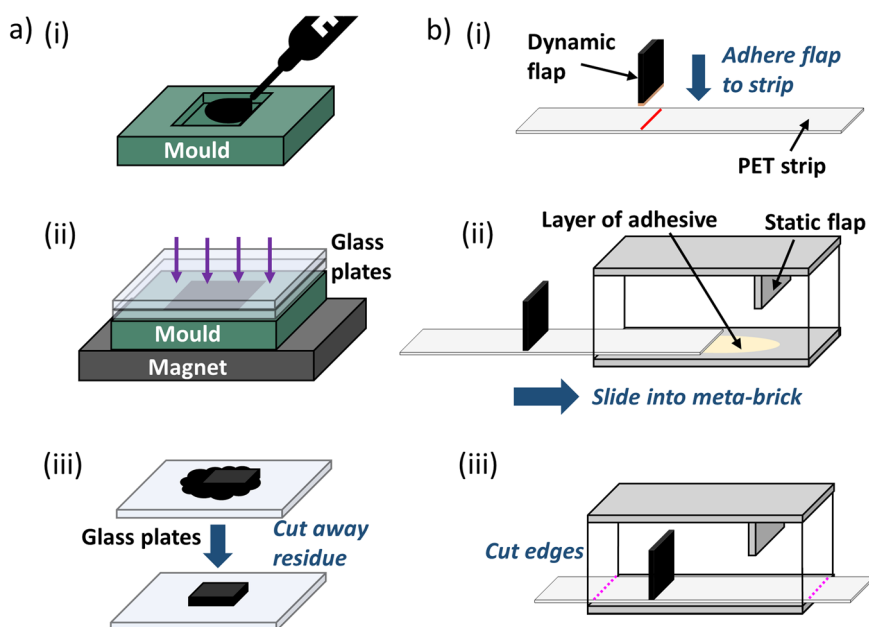

Fig. 2 Fabrication of magnetic flap and assembly process of dynamic meta-brick. a Schematics of moulding method. (i) Dispensing magnetic mixture in 3D-printed mould, (ii) Two glass plates on top of mould and placing mould on magnet, (iii) Cured flap on glass plate, and flap after residue is cut away. **b** Schematics of assembly method. (i) Flap is adhered to PET strip (thickness, 100 μm). The liquid glue coating is shown as orange colour at the bottom tip of the flap. The red line marks the predetermined position to glue the flap approximately 2.6 mm from the meta-brick inlet. (ii) PET strip with the flap attached is inserted into meta-brick, (iii) Excess edges of PET strip is cut away.

Supplementary Information) This designed clearance is much smaller than the wavelength of 8.66 mm, therefore any acoustic discrepancies observed during operation were negligible.

Our alternative film-based assembly is advantageous because it allowed accurate placement of the flap with tight tolerances, while still allowing the meta-brick to be monolithically printed. For increased production volume, the pieces of the PET film could be easily laser-cut with slits to mark the positions of the flaps. Beyond the assembly of our meta-bricks, this technique could be applied to other applications which necessitate the integration of structures within narrow spaces.

After assembly, the dynamic meta-brick, was actuated by a permanent magnet. Figure 1b depicts the binary action in the actuated (A1) and unactuated (A0) states. Upon actuation, the flap rapidly moved towards the wall. In the presence of the magnetic field, the actuated flap state (A1) was sustained and stable. When unactuated by removing the magnetic stimulus, the flap automatically resumed its original state (A0). See Supplementary Movie 2 for a visual description of the fabrication process.

Binary ultrasonic modulation. Figure 3 shows the simulated (COMSOL Multiphysics®) and experimental YZ plots for phase (rad). State A1 has a smaller phase shift (relative to the transducer phase) of 0.50 rad, as compared to state A0 with a shift of 1.63 rad. State A0 has a higher phase shift because it has a longer effective path length compared to state A1, which leads to a longer propagation time, which is a result of the obstructing dynamic flap positioned normal to the direction of wave propagation. Beyond the difference in the phase, we also noticed an effect on amplitude, when the dynamic meta-brick was actuated. A difference of 4.7 dB was obtained between the states, with state A1 showing higher transmission than state A0. (see Supplementary Note 2, Supplementary Information).

To investigate how a combination of actuation states affects transmission in a small dynamic array, we iterated the dynamic meta-brick to form a two-brick array. The schematics in Fig. 4 illustrate how the two meta-bricks were arranged together to enable symmetry and ease of actuation by rotating one of the meta-bricks. In this configuration, the actuating magnet could

easily access the meta-brick wall attached with the magnetic flap. For both simulations and experiments, the YZ plots for the actuation of the dynamic flap on the left meta-brick (state [1 0]) depicts the shape of the transmitted beam with uneven actuation. Here, the uneven actuation caused a phase gradient. (see Supplementary Note 2, Supplementary Information) This phase gradient translated into the positioning of the main beam towards the right of the centre of the acoustic pressure plots (shown by the vertical dotted black line at $y = 0$) by 3 ± 1 mm, along with concentrated transmission through the actuated left brick, as plotted in the line plot (Fig. 4). The line plot shows the uneven amplitude profile of the beam, where transmission is higher on the right. This uneven profile is compared to the case where both flaps are actuated (state [1 1]), shown by the YZ plots, and the corresponding pink line in the line plot. As the array is symmetrical, the opposite is true where actuation on the right would cause a shift of the beam towards the left.

Both simulations and experiments show good agreement. However, there are losses in experiments which are reflected in the amplitude line plot, with a difference of approximately 6 dB in comparison with the simulated data (Fig. 4). These losses could be attributed to the environment, such as unwanted reflections from the table or possibly thermoviscous effects. At ultrasonic frequencies, it has been reported that these effects could cause transmission loss, although the impact on phase is minimal[52].

Meta-brick stacks and metasurfaces. Each meta-brick allows a certain phase shift. When the meta-bricks are physically combined together into a metasurface, their combined phase shifts form a collective acoustic output. A desired output sound field can be achieved by pre-defining the phase values, i.e., determining what type of meta-brick is required, and their placement relative to one another.

In this work, we demonstrate that the inclusion of a small number of locally actuated dynamic meta-bricks can make an otherwise static global metasurface operate dynamically. We showcase several degrees of reconfigurability with a composite hybrid static-dynamic metasurface. First, we are able to control the magnetic flap within the dynamic meta-brick. Second, the
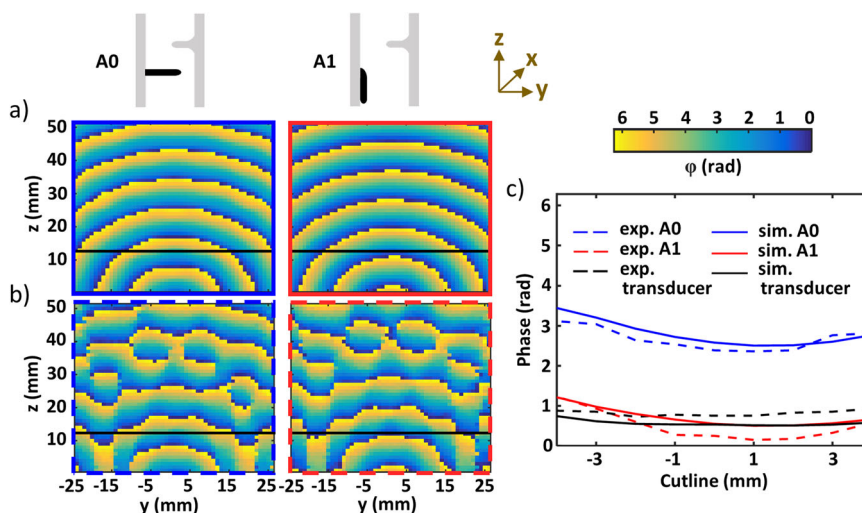

Fig. 3 Modulation of phase according to the actuation state for an individual dynamic meta-brick. a Simulated and **b** Experimental YZ plots showing phase (rad) for unactuated (A0) and actuated (A1) states. Corresponding meta-brick schematics are shown above the plots. The horizontal black solid lines in all the YZ plots marks the location of a 50 mm long horizontal cutline, positioned at a vertical distance of 17 mm, which is approximately two wavelengths from the output of the meta-brick. **c** The line plot compares simulated and experimental phase (rad) plotted against a short section (~1λ) of the horizontal cutline. Dashed lines represent experimental results, and solid lines represent simulated results, matching the border of the YZ plots. Results for A0 is shown in blue, A1 is shown in red, and the transducer sound source output without the meta-brick is shown in black.
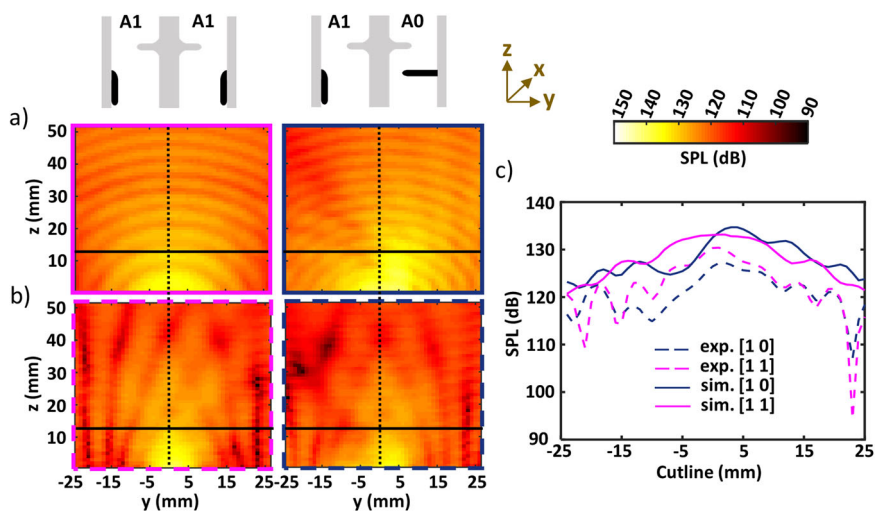
Fig. 4 Modulation of transmission amplitude according to the actuation state for an array of two meta-bricks. a Simulated and **b** Experimental YZ plots showing acoustic sound pressure level (SPL, dB) for the two-brick array. According to the corresponding meta-brick schematics, state [1 1] shows that both flaps are actuated, and state [1 0] shows that only the left flap is actuated. The horizontal black solid lines in all the YZ plots marks the location of a 50 mm long horizontal cutline, positioned at a vertical distance of 17 mm, which is approximately two wavelengths from the output of the meta-bricks. The vertical dotted black line marks the centre of the plots. **c** The line plot shows sound pressure level (SPL, dB) for the two-brick array, plotted against the full length of the horizontal cutline. Dashed lines represent experimental results, and solid lines represent simulated results. The dark blue lines represent state [1 0]. The pink lines represent state [1 1].

dynamic meta-bricks can be assembled within a metasurface layer mainly comprising static meta-bricks. Third, the metasurface layer which consists of the dynamic meta-bricks can be assembled with another metasurface layer through 'stacking', by setting the meta-bricks on top of one another. Structurally and computationally, the integrated hybrid metasurface is formed from the concatenation of meta-brick stacks. Forming meta-brick stacks is a practical and effective method to make a metasurface more compact with enhanced functionalities.

Memoli et. al.[4] reported fully stacked metasurfaces with the purpose of reducing the number of distinct phases required to achieve a certain spatial sound field, for applications like a steered beam and levitation of a bead. However, their metasurface was fully static, based on a set of 16 static meta-brick designs with distinct phase delays. We add a new dimension to this, by building stacks with dynamic meta-bricks which provides pairs of phases that can display different outputs depending on the actuation states. There are two main types of stacks: a "static" and a "dynamic hybrid" stack. "Static" stacks are formed from placing a static meta-brick on top of another static meta-brick. "Dynamic hybrid" stacks are formed from a combination of dynamic and static meta-bricks. Figure 5a shows how stacking a dynamic meta-brick on top of a given static meta-brick, can render any static meta-brick into a dynamic meta-brick with binary states, by creating a kind of vertical super-cell.

Before making the metasurface, we ensured that the dynamic meta-bricks were suitable to be integrated within a large array. For the individual or two meta-brick measurements, it was sufficient for the cross-sectional dimensions (i.e., width and length) to be subwavelength, less than $\lambda = 8.66$ mm. In a metasurface with hundreds of meta-bricks, the dynamic meta-brick would be surrounded by other meta-bricks, and it is important for the width and length to be at least $\lambda/2 = 4.33$ mm or less to reduce distortions in the output sound field[8,53]. Hence, the dimensions were modified as such, for better integration of the meta-bricks within a large array. (see Supplementary Note 3, Supplementary Information) Additionally, the magnetic flux
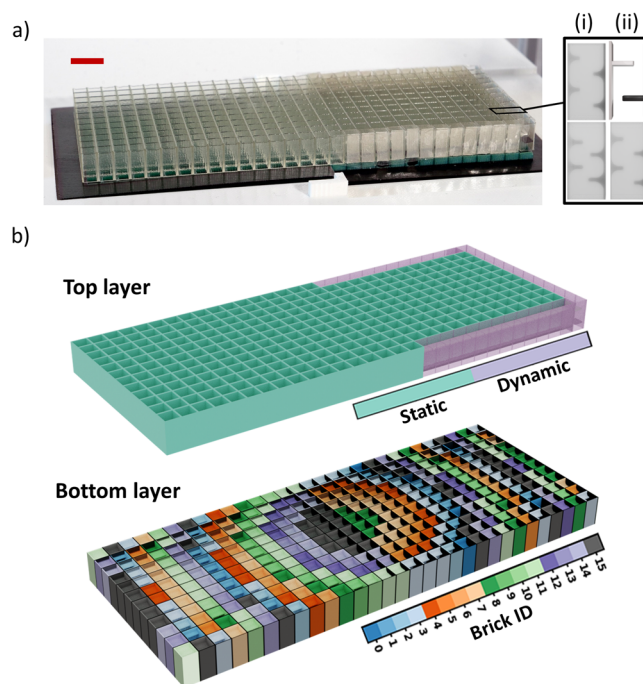

Fig. 5 An illustration of meta-brick stacks, and the respective layers in the metasurface. a Photograph of stacked metasurface layers and inset showing (i) "static" and (ii) "dynamic hybrid" meta-brick stacks. Scale bar, 1 cm. **b** 3D maps for top and bottom metasurface layers. The 'top layer' map shows the dynamic meta-bricks (purple) located along the edge of the metasurface. The fully static 'bottom layer' map shows the meta-brick identifications (ID) (based on a set of 16 static meta-bricks) and corresponding locations of the assembled static meta-bricks.

density from the permanent magnets was not strong enough to reach the centre of the metasurface. Therefore, we situated the dynamic hybrid stacks at the edges of the metasurface.
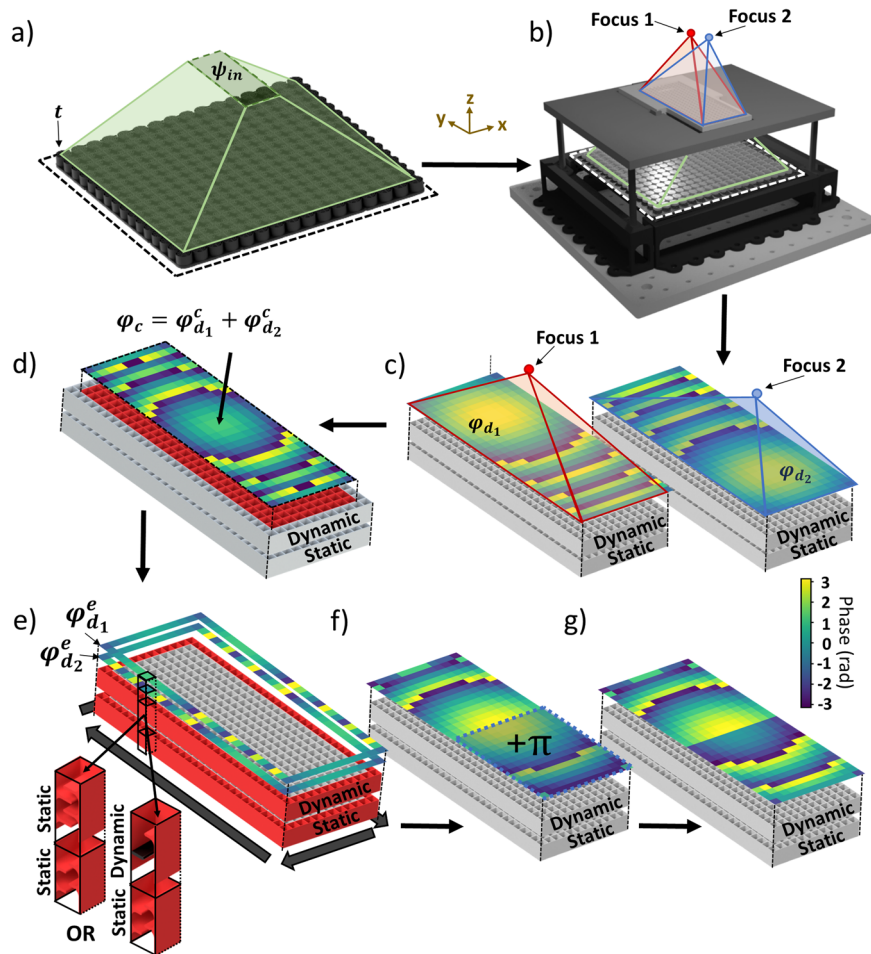
Fig. 6 Schematic process flow of phase retrieval algorithm. a Each transducer t contributes to the complex pressure ψ_{in} incident on the underside of the AMM. **b** The dynamic metasurface stack focuses at two different points when the dynamic meta-bricks are actuated and unactuated respectively. **c** We create a stack of static and dynamic metasurfaces to generate the two focal points. Note that the focal points are not drawn to scale in the schematics. **d** We average the central bricks as these must remain static. **e** For the edge bricks, we step through brick-by-brick to determine if a fully static stack or a static-dynamic hybrid stack is more suitable at this particular location. **f** We add π to half of the metasurface to turn our focus into a twin trap. **g** Output of the algorithm.

Dynamic acoustic twin traps. As proof-of-concept, we intended to design the composite stacked metasurface (Fig. 5) to demonstrate focussed beams in the form of acoustic twin traps. A twin trap can be understood as a split focus, where a phase of π is added to half of the phase responses of the metasurface to generate a focal point (Fig. 6). The twin trap would be horizontal[54], where an outer regime of high acoustic pressure characterised by two focussed high pressure lobes surrounds a region of low acoustic pressure.

The composite stacked metasurface would generate a pair of dynamic twin traps which could shift according to the actuation state of the assembled dynamic meta-bricks. Twin traps generated by PAT systems may merge together when they are positioned in close proximity. To prevent the traps from merging, Marzo et al.[55] used a minimum distance of 1.4λ between adjacent twin traps projected at the same time. As our acoustic output is produced by an acoustic metasurface, we wanted to demonstrate a smaller distance of $\lambda/4 \approx 2$ mm to see if distinct spatial traps could be visualised when projected sequentially without merging. Moving twin traps at millimetre-scale distances is commonly applied for biomedical applications[56].

Finding the optimal combinations of meta-bricks and their stacks was an essential step to design the metasurface for the dynamic twin traps. The optimisation process required the identification of the type of meta-brick (different meta-bricks providing different phase values), and the positioning of the specific static and dynamic meta-bricks. In particular, for this application we wanted to place the dynamic meta-bricks at the edges of the metasurface. To achieve this, we developed a constrained phase retrieval algorithm (Fig. 6) (see Methods) that: (1) determined which meta-bricks should be static and which should be dynamic, and for locations containing a static meta-brick, (2) found which of the 16 distinct brick designs were required, and (3) minimised the number of dynamic meta-bricks, while retaining the functionality of the device. We implemented the algorithm to generate the composite stacked device with an optimised number of 36 "dynamic hybrid" meta-brick stacks. The bottom metasurface layer consisted of purely static meta-bricks, while the top layer consisted of static bricks together with a handful of 36 assembled dynamic meta-bricks along the right-hand edge of the metasurface (Fig. 5b).

Figure 7 shows the experimental and simulated results for the generated twin traps. The simulated and experimental results were in excellent agreement, with a shift of approximately 1.7 ± 0.2 mm. We actuated the dynamic meta-bricks at the edges of a composite stacked metasurface at the same time using a permanent magnet-based horse-shoe structure (see Supplementary Movie 1) to provide an invariable uniform magnetic field
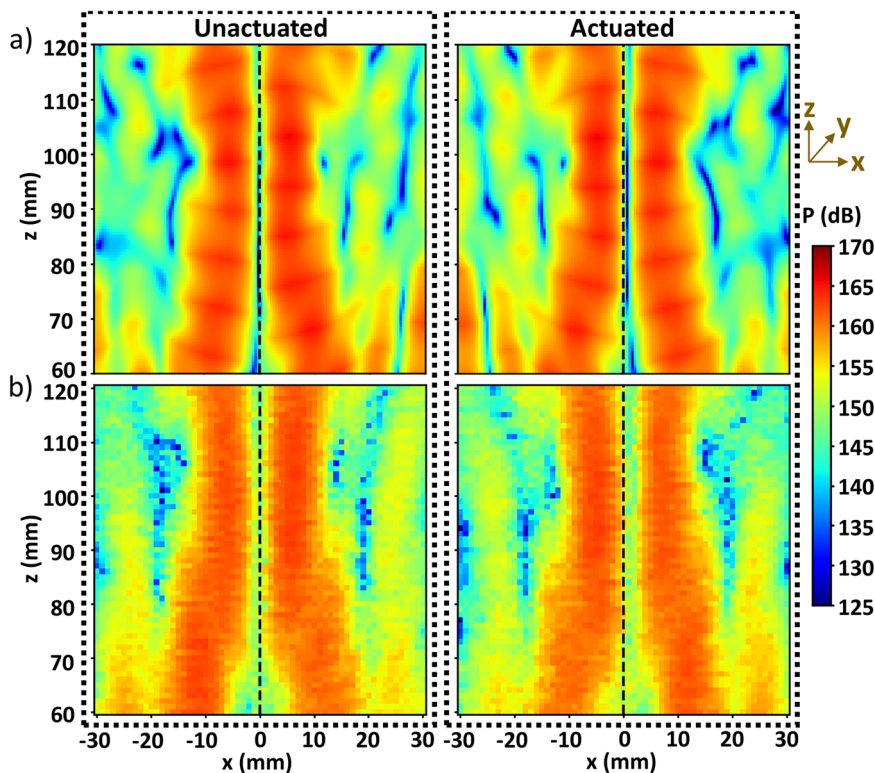
Fig. 7 Acoustic twin traps generated by the metasurface. a Simulated and **b** experimental XZ pressure plots in dB, showing the position of the twin traps when the dynamic meta-bricks are in the unactuated and actuated states. The vertical dashed black lines mark the centre of the plot. The trap can be seen to shift with respect to the dashed lines.

during actuation. Within the horse-shoe structure, identical magnets are placed side-by-side. A single magnet interfaces with three dynamic meta-bricks (see Supplementary Fig. 5, Supplementary Information). In one actuation state, a twin trap was generated at a distance of 12λ from transducer board. Upon actuation, we successfully created another twin trap at a distance of $\sim \lambda/4$ towards the right from the earlier trap in real-time, which highlighted the precision of the metasurface. We also used a reflector plate to increase the strength of the twin traps. The sound source used for providing the acoustic field was a 16×16 phased array transducer (PAT) board, which was driven at 20 V. All the transducers were well-calibrated beforehand and were turned ON with a zero mutual phase difference. Acoustic pressure measurements were taken within a $100\,mm \times 100\,mm$ scan size. The metasurface was placed within 3D-printed support structures (see Supplementary Fig. 6, Supplementary Information).

Dynamic acoustic levitation. The pressure measurements in Fig. 7 were obtained at the two instances when the metasurface was actuated and unactuated, however we were unable to visualise the real-time modulation of the sound field. Within a twin trap, the balance of acoustic pressure can tweeze objects[55,57] at the low acoustic pressure region. Therefore, for further experimental validation, we shifted a lightweight polystyrene bead (~3.3 mm diameter) between the two twin traps (Fig. 8). (see Supplementary Movie 1). Upon actuation, the twin trap, along with the bead, laterally moved towards the right by a distance of approximately 1.3 ± 0.4 mm. The bead did not drop during actuation, which indicated that the sound field was modulating fast enough to maintain levitation.

Discussion

With the introduction of dynamic meta-bricks, this work presented a paradigm to design dynamic AMMs. AMMs are composed of unit cells, and the nature of these unit cells determines the nature of the full device. If all the unit cells are static, the full AMM would also be static. Therefore, AMMs which produce a dynamic output have been traditionally constructed with fully dynamic/active unit cells[17,40,58]. Here, we challenged this notion by advocating for hybrid static-dynamic designs, through our transmissive space-coiling unit cell (i.e., meta-brick).

We demonstrated that the inclusion of a single, small dynamic magnetic flap can transform a static meta-brick into a dynamic meta-brick. Within the dynamic meta-brick, we used a combination of the static flap, and the actuation state of the magnetic flap to produce more than one output. The static and dynamic flaps were of different lengths. Between the two binary actuation states for an individual dynamic meta-brick design, we created a prominent phase difference of 2.14 rad, and recorded an output pressure difference of 4.7 dB. These results indicate that there are many combinations of parameters yet to be explored for the design of dynamic meta-bricks (or space-coiling geometries in general).

Our dynamic meta-brick could pave the way for more sophisticated designs. Currently, only a portion of the path length is dynamic. For instance, increasing the number of static or controllable flaps would allow smaller phase shifts, and more precise channel alterations. The same principle would apply to a larger meta-brick for the audible regime, which would have a wider range of suitable actuation techniques. For example, moving away from the cantilever concept, the space-coiling path length could have a labyrinth of static or dynamic inflated/deflated pneumatic protuberances. The design process for new
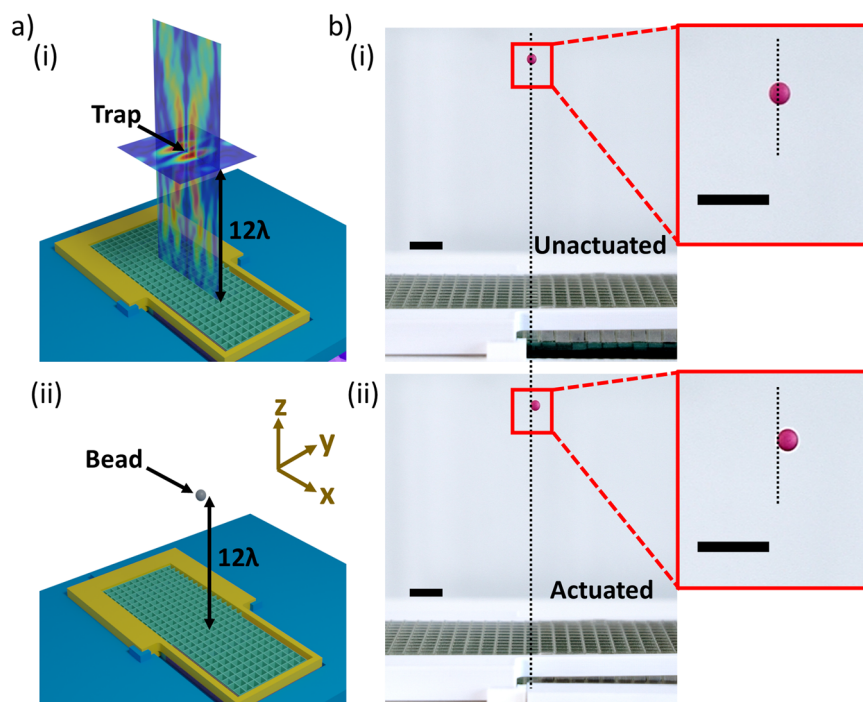
Fig. 8 Results of dynamic acoustic levitation. a Schematics showing (i) two measurement planes (horizontal and vertical) of a twin trap, and the corresponding (ii) bead which is trapped at the cross-section of the two planes. **b** Photographs of levitated bead (pink colour) in two states, unactuated and actuated, with insets outlined in red. Scale bars, 1 cm. The vertical dotted line is for visualisation.

geometries could also be streamlined using computational optimisation algorithms combined with machine learning[59,60]. Currently a main limitation of our ultrasonic dynamic meta-bricks is that they can only be accessed by permanent magnets from the side. In the future, possible improvements to the design would be to change the permanent magnets to electromagnets, and/or change the magnetite particles to hard magnetic particles such as neodymium iron boron for the MRE flap. With magnetic alignment, hard magnetic particles could improve the responsivity of the flap[61]. With the use of electromagnets, a varied magnetic field could be generated to possibly actuate the bulk of the metasurface. Similar setups with external orthogonal electromagnets have been used in soft robotics to enable complex programmable motion and locomotion[35] to target locations from a distance. Furthermore, there has been an increase in the use of thin-film or soft electromagnetic coils/actuators[62,63] in recent years, which could possibly be integrated into the metasurface (e.g., on the meta-bricks walls, flaps, or surrounding support structures).

In this work we also showcased how dynamic meta-bricks can be combined with other meta-bricks. A small array of two dynamic meta-bricks could shape the beam according to phase gradient through selective actuation. A dynamic meta-brick stacked with any static meta-brick created a "dynamic hybrid" stack, which could offer a wide, controlled variation of phase values upon concatenation in a metasurface. Through stacking, we formed a composite metasurface from a combined assembly static and dynamic meta-bricks. The hybrid composition of the metasurface allowed the same assembly configuration to output two distinct acoustic field patterns based on the actuation state of the dynamic meta-bricks. We demonstrated spatially controllable acoustic twin traps, which were physically visualised by shifting a tweezed bead in mid-air between them. Our experimental results were understood using a theoretical model (phase design algorithms) and through COMSOL Multiphysics® simulations, and the results were in excellent agreement.

Primarily, our demonstration with the metasurface proved that global operational dynamicity is achievable without a fully dynamic metasurface. In our case, only a set of dynamic meta-bricks situated along the edges were controllable. Our stacked metasurface was computationally designed to exhibit accuracy on the scale of millimetres, to move twin traps between a distance of $\lambda/4 \approx 2$ mm. Despite the close proximity of the twin traps locations, they were measured as visibly distinct. Moreover, the sound field modulated fast enough for the bead to move between traps without dropping. Notwithstanding the low dynamicity ratio where dynamic to static meta-bricks were 1:9 within the metasurface, dynamic acoustic levitation was implemented without the electronic complexity of PAT-based[41] systems.

Within the stacked metasurface, the dynamic edge bricks were all actuated/unactuated together. To expand the possible output pressure fields within a single metasurface beyond binary modulation, future designs could have a greater variation in actuation patterns for the dynamic meta-bricks, where groups, pairs, or individual meta-bricks (see Supplementary Movie 3) could have different actuation states during operation. Highly localised, selective, and collective actuation would allow efficient deployment for fixed patterns, similar to the versatility of ubiquitous optical seven-segment displays[64]. Here, in particular, multifunctional (i.e., allows multiple functions using the same device such as acoustic switching, levitation, beam focussing, etc.) AMMs which are reconfigurable in real-time could advance existing haptic technology (e.g., for virtual reality/ augmented reality applications[45]). Such AMMs could also enable holographic projections for applications like acoustic energy harvesting[44].

In this work, we presented different fabrication processes, namely, silicone moulding using resin-printed moulds with a technique to treat curing inhibition, and a film-based method to assemble small objects (like the flaps) within narrow, inaccessible spaces. The former, can be explored as an alternative to the use of commercial sprays (e.g., Inhibit X™) or baking treatments[65] before silicone moulding, with possible uses in diverse fields such

as robotics, microfluidics, metamaterials, archaeology, and medicine, etc. to fabricate moulds, models, or parts. The latter, has implications for the integration of objects like circuitry such as sensors and antennas, or actuators, within confined spaces. For instance, our method can be used to insert a small electronic chip which may need to be secured within a long narrow aperture (difficult to reach with tweezers), as part of a robotic system. Further, actuators, like our flaps, can be functionalised, patterned, or coated (e.g., conductive ink[66], or mechanoluminescent[67] powder) before assembly, to provide additional functionalities. Our fabrication processes could be especially useful in facilitating active reconfigurability within soft pneumatic, soft robotic, or fluidic systems which often use actuatable components[68,69] like valves.

Moving forward, we believe that adopting an interdisciplinary, integrated, and modular approach towards actively and passively reconfigurable components (e.g., metamaterial unit cell), could pave the way for the development of next-generation metamaterials.

Methods

Materials and fabrication of passive components. All passive components were designed using the Autodesk® Inventor® Professional software. The meta-brick shells, including the internal static flaps, were 3D-printed (Stratasys J750 multi-material Polyjet) in the transparent VeroClear™ material. Due to the presence of overhangs, the meta-bricks were printed with water-soluble support material (SUP706). Moulds and frames were printed using LCD-based Digital Light Processing (DLP, Phrozen Sonic Mini 4 K and Anycubic Photon Mono X). The DLP prints were washed in isopropyl alcohol (IPA), and UV-cured (405 nm LED) in the AnyCubic Wash & Cure Machine 2.0. The moulds required additional post-processing steps as they were being used for silicone casting. To remove any polar, non-polar, and heat labile inhibitors which could disrupt the curing process[65], the moulds were washed in a mixture of 70% ethanol and 30% IPA and later washed in de-ionised (DI) water. The ethanol mixture and DI water were split into smaller beakers (at least three each) for sequential washing for a greater dilution effect. The final step involved soaking the Siraya tech-resin moulds within a large bowl of water (approx. 1.5 L) with a temperature within the range of >50 °C and <67 °C for an hour. A combination of washing in alcohol, DI water, and submersion in hot water, reproducibly eliminated the curing inhibition. Our approach to prevent curing inhibition is quick and straightforward without needing specialised equipment or high temperatures. The frames for pressure measurements for the meta-bricks were printed using Anycubic Clear UV 405 nm resin. All support structures were printed via Fused-Deposition Modelling (FDM, Prusa i3, MK3S) using Polylactic acid (PLA), a type of biodegradable thermoplastic.

Fabrication and magnetic actuation of elastomeric flap. The magnetorheological elastomeric flap was manufactured via moulding and casting[51] (see Supplementary Movie 2). Ecoflex™ 00-30 and synthetic magnetite (Fe_3O_4) nanoparticles (diameter, ~0.20 μm) (Inoxia Ltd) were mixed together, desiccated, and air-cured overnight within a mould in the presence of an external magnetic field (~160 mT) provided by neodymium (NdFeB) magnets with dimensions of 50 mm × 10 mm × 5 mm. For actuation, a single stackable N42 neodymium magnet (at least 360 mT) (see Supplementary Fig. 5, Supplementary Information) had dimensions of 12 mm × 4 mm × 5 mm. After >1000 actuations, there was no sign of breakage of the flap.

Simulations for dynamic meta-brick. Numerical simulations were carried out in the commercial software COMSOL Multiphysics®, Version 5.4. Under the Acoustics Module, our frequency-domain acoustic pressure models were based on the Finite Element Method (FEM), which is effective for small, closed-air domains. The piston model formula[8] was applied to model the acoustic pressure input from a physical ultrasonic transducer for an operating frequency of 40 kHz. The speed of sound was set to 346.4 m/s (dry air, 25 °C). To model, the high impedance contrast between different materials, i.e., air, plastic, silicone, internal hard boundary conditions were applied to the walls and flap surfaces. External hard boundary conditions were applied on all the external walls. Perfectly matched layers (PML) were placed at the outer edges of the surrounding air domain, which act as absorptive non-reflective boundaries. Our dynamic flaps have discrete binary states, and 3D simulations were mainly conducted to obtain data for the amplitude and phase of acoustic wave propagation.

With a 2D model, a series of parameter sweeps (see Supplementary Note 4) were executed to optimise the geometry of the meta-bricks. This iterative approach was primarily employed in favour of speed and efficiency because it allowed us to quickly narrow down the range of dimensions to construct the bricks. The geometric restrictions enforced by the physical meta-brick geometry (e.g., order of magnitude of dimensions; height of the brick, thickness of the walls, length of flaps, etc.) defined the types of parameters and range of parameter values, which were controlled using the COMSOL Multiphysics® in-built 'parametric sweep' functionality.

Transmission measurements. For pressure measurements, the meta-bricks were assembled within 3D-printed frames, which were then fitted within a support structure (see Supplementary Fig. 4, Supplementary Information). The frame was designed with tight tolerances, which allowed the device to be placed in any orientation without the meta-bricks shifting or falling out from their positions.

An ultrasonic 40 kHz transducer (MA40S4S, Murata Electronics, Japan) was placed at a distance of one wavelength away from the input of the meta-bricks, emitting waves at the central operating frequency of 40 kHz. The transducer was driven at a voltage of 20 V_{pp} by a sinusoidal input provided by a GW Instek AFG-2225 dual-channel arbitrary function generator. A receiver scanned the surrounding measurement area with a scan size of 50 mm × 50 mm. The receiver was a Brüel & Kjær 4138-a-015 microphone that was attached to a CNC linear stage for scanning. To scan the YZ plane, the microphone was positioned 5 mm away from the AMM in the z-direction. A Brüel & Kjær 2670 preamplifier was used with the microphone, which was externally polarised. The signals were stored digitally through a PicoScope 4262 for analysis to obtain the quantitative amplitude and phase measurement data, which were plotted in MATLAB®. The transmitted pressure was normalised according to (dB) = 20 log(P_m/P_0), where P_m and P_0 (10^{-6} Pa) are the measured and reference acoustic pressures respectively.

Constrained phase retrieval algorithm. The steps of the algorithm are as follows:

1. First, we find the complex pressure distribution ψ_{in} incident on the underside of the metasurface stack using the transducer piston model (see Supplementary Note 5).
2. Next, we find the two sets of analogue phase delay values (φ_{d1} and φ_{d2}) that the AMM device must apply to the incident phase $\varphi_{in} = \mathbf{angle}(\psi_{in})$ in its two configurations to

generate focal points in two locations. We find these using a simple Pythagorean matrix calculation (see Supplementary Note 6).

3. The central stacks in the device must be static, as the external magnet used to activate dynamic bricks cannot reach them. So here, we take the circular mean of the central section φ_d^c across the two modes of the device such that $\varphi^c = \varphi_{d_1}^c + \varphi_{d_2}^c$ and create the corresponding "static" stacks.

4. For the edge stacks, we step through each of the elements on a stack-by-stack basis and calculate whether they should be static or dynamic. If the difference between φ_{d1} and φ_{d2} at some edge position is close to that offered by a "dynamic hybrid" stack, then we create that stack here. Elsewise, if averaging and keeping both bricks static allows this stack to stay closer to φ_{d1} and φ_{d2} then we keep it static.

5. By averaging the central bricks and calculating all the edge bricks, we identify a full stacked metasurface which tells us the required positions and types of each static and dynamic brick to create focal points in the two chosen locations. Switching the dynamic bricks between states gives us two new and distinct phase delay maps (φ_{d1}' and φ_{d2}') for the two configurations.

6. The final step is to add a constant additional phase of π to one-half of each phase delay map to create the twin trap signature in each case (φ_{t1} and φ_{t2}). The twin trap signature splits the focal point generated by each mode into two trapping points separated by half a wavelength.

Simulations for metasurface stacks. In order to simulate the output pressure distributions, we recombine the phase delay maps describing the two modes of the metasurface stack (φ_{t1} and φ_{t2}) with ψ_{in} to create modulated pressure distributions for each mode $\psi_{mod} = a_{in} \cdot e^{i(\varphi_{in}+\varphi_t)}$. We can propagate these pressure distributions into the far field using the angular spectrum method (see Supplementary Note 7) to give predictions for the acoustic pressure distributions output by the two modes of the device.

Data availability
The data is available from the authors upon reasonable request.

References
1. Norasikin, M. A. et al. SoundBender. In *Proc. 31st Annual ACM Symposium on User Interface Software and Technology* 247–259 (ACM, 2018).
2. Esfahlani, H., Karkar, S., Lissek, H. & Mosig, J. R. Acoustic carpet cloak based on an ultrathin metasurface. *Phys. Rev. B* **94**, 014302 (2016).
3. Zigoneanu, L., Popa, B.-I. & Cummer, S. A. Three-dimensional broadband omnidirectional acoustic ground cloak. *Nat. Mater.* **13**, 352–355 (2014).
4. Memoli, G. et al. Metamaterial bricks and quantization of meta-surfaces. *Nat. Commun.* **8**, 14608 (2017).
5. Tian, Z. et al. Programmable acoustic metasurfaces. *Adv. Funct. Mater.* **29**, 1808489 (2019).
6. Tian, Y., Wei, Q., Cheng, Y. & Liu, X. Acoustic holography based on composite metasurface with decoupled modulation of phase and amplitude. *Appl. Phys. Lett.* **110**, 191901 (2017).
7. Xie, Y. et al. Acoustic holographic rendering with two-dimensional metamaterial-based passive phased array. *Sci. Rep.* **6**, 35437 (2016).
8. Prat-Camps, J., Christopoulos, G., Hardwick, J. & Subramanian, S. A manually reconfigurable reflective spatial sound modulator for ultrasonic waves in air. *Adv. Mater. Technol.* **5**, 2000041 (2020).
9. Bansal, S. & Subramanian, S. A microfluidic acoustic metamaterial using electrowetting: enabling active broadband tunability. *Adv. Mater. Technol.* **6**, 2100491 (2021).
10. Airoldi, L. & Ruzzene, M. Design of tunable acoustic metamaterials through periodic arrays of resonant shunted piezos. *New J. Phys.* **13**, 113010 (2011).
11. Casadei, F., Delpero, T., Bergamini, A., Ermanni, P. & Ruzzene, M. Piezoelectric resonator arrays for tunable acoustic waveguides and metamaterials. *J. Appl. Phys.* **112**, 064902 (2012).
12. Zhou, W., Wu, Y. & Zuo, L. Vibration and wave propagation attenuation for metamaterials by periodic piezoelectric arrays with high-order resonant circuit shunts. *Smart Mater. Struct.* **24**, 065021 (2015).
13. Baz, A. Active acoustic metamaterial with tunable effective density using a disturbance rejection controller. *J. Appl. Phys.* **125**, 074503 (2019).
14. Tang, Y.-F., Liang, B., Yang, J., Yang, J. & Cheng, J. Voltage-controlled membrane-type active acoustic metasurfaces with ultrathin thickness. *Appl. Phys. Express* **12**, 064501 (2019).
15. Chen, X. et al. Active acoustic metamaterials with tunable effective mass density by gradient magnetic fields. *Appl. Phys. Lett.* **105**, 071913 (2014).
16. Tang, X. et al. Magnetoactive acoustic metamaterials based on nanoparticle-enhanced diaphragm. *Sci. Rep.* **11**, 1–8 (2021).
17. Ma, G., Fan, X., Sheng, P. & Fink, M. Shaping reverberating sound fields with an actively tunable metasurface. *Proc. Natl. Acad. Sci. USA* **115**, 6638–6643 (2018).
18. Malinovsky, V. S. & Donskoy, D. M. Electro-magnetically controlled acoustic metamaterials with adaptive properties. *J. Acoust. Soc. Am.* **132**, 2866–2872 (2012).
19. Chen, Z. et al. A tunable acoustic metamaterial with double-negativity driven by electromagnets. *Sci. Rep.* **6**, 30254 (2016).
20. Assouar, B. et al. Acoustic metasurfaces. *Nat. Rev. Mater.* **3**, 460–472 (2018).
21. Liang, Z. & Li, J. Extreme acoustic metamaterial by coiling up space. *Phys. Rev. Lett.* **108**, 114301 (2012).
22. Fu, X. F., Li, G. Y., Lu, M. H., Lu, G. & Huang, X. A 3D space coiling metamaterial with isotropic negative acoustic properties. *Appl. Phys. Lett.* **111**, 251904 (2017).
23. Liang, Z. et al. Space-coiling metamaterials with double negativity and conical dispersion. *Sci. Rep.* **3**, 1614 (2013).
24. Liu, C., Xia, B. & Yu, D. The spiral-labyrinthine acoustic metamaterial by coiling up space. *Phys. Lett. A* **381**, 3112–3118 (2017).
25. Liu, J., Li, L., Xia, B. & Man, X. Fractal labyrinthine acoustic metamaterial in planar lattices. *Int. J. Solids Struct.* **132–133**, 20–30 (2018).
26. Azbaid El Ouahabi, A. & Memoli, G. A transfer matrix method for calculating the transmission and reflection coefficient of labyrinthine metamaterials. *J. Acoust. Soc. Am.* **151**, 1022–1032 (2022).
27. Xie, Y. et al. Wavefront modulation and subwavelength diffractive acoustics with an acoustic metasurface. *Nat. Commun.* **5**, 5553 (2014).
28. Zangeneh-Nejad, F. & Fleury, R. Active times for acoustic metamaterials. *Rev. Phys.* **4**, 100031 (2019).
29. Sun, M. et al. Reconfigurable magnetic slime robot: deformation, adaptability, and multifunction. *Adv. Funct. Mater.* **32**, 2112508 (2022).
30. Wang, X. et al. Untethered and ultrafast soft-bodied robots. *Commun. Mater.* **1**, 67 (2020).
31. Mao, G. et al. Ultrafast small-scale soft electromagnetic robots. *Nat. Commun.* **13**, 4456 (2022).
32. Bastola, A. K., Paudel, M., Li, L. & Li, W. Recent progress of magnetorheological elastomers: a review. *Smart Mater. Struct.* **29**, 123002 (2020).
33. Jiang, S. et al. Multifunctional janus microplates arrays actuated by magnetic fields for water/light switches and bio-inspired assimilatory coloration. *Adv. Mater.* **31**, 1807507 (2019).
34. Lum, G. Z. et al. Shape-programmable magnetic soft matter. *Proc. Natl. Acad. Sci. USA* **113**, E6007–E6015 (2016).
35. Hu, W., Lum, G. Z., Mastrangeli, M. & Sitti, M. Small-scale soft-bodied robot with multimodal locomotion. *Nature* **554**, 81–85 (2018).
36. Ren, Z., Hu, W., Dong, X. & Sitti, M. Multi-functional soft-bodied jellyfish-like swimming. *Nat. Commun.* **10**, 1–12 (2019). *2019 101*.
37. Willey, C. L., Chen, V. W., Scalzi, K. J., Buskohl, P. R. & Juhl, A. T. A reconfigurable magnetorheological elastomer acoustic metamaterial. *Appl. Phys. Lett.* **117**, 104102 (2020).
38. Yu, K., Fang, N. X., Huang, G. & Wang, Q. Magnetoactive acoustic metamaterials. *Adv. Mater.* **30**, 1706348 (2018).
39. Lee, K. H. et al. Sharkskin-inspired magnetoactive reconfigurable acoustic metamaterials. *Research* **2020**, 1–13 (2020).
40. Ma, Z. et al. Spatial ultrasound modulation by digitally controlling microbubble arrays. *Nat. Commun.* **11**, 4537 (2020).
41. Hirayama, R., Martinez Plasencia, D., Masuda, N. & Subramanian, S. A volumetric display for visual, tactile and audio presentation using acoustic trapping. *Nature* **575**, 320–323 (2019).
42. Hirayama, R., Christopoulos, G., Plasencia, D. M. & Subramanian, S. High-speed acoustic holography with arbitrary scattering objects. *Sci. Adv.* **8**, 7614 (2022).
43. Plasencia, D. M., Hirayama, R., Montano-Murillo, R. & Subramanian, S. GS-PAT. *ACM Trans. Graph.* **39**, 138:1–138:12 (2020).

44. Bansal, S. et al. Transmissive labyrinthine acoustic metamaterial-based holography for extraordinary energy harvesting. *Adv. Eng. Mater.* **25**, 2201117 (2022).

45. Yang, T. et al. Recent advances and opportunities of active materials for haptic technologies in virtual and augmented reality. *Adv. Funct. Mater.* **31**, 2008831 (2021).

46. Memoli, G. et al. Vari-Sound: a varifocal lens for sound. In *Proc. Conference on Human Factors in Computing Systems* 1–14 (ACM, 2019).

47. Kepa, M. W. et al. Acoustic levitation and rotation of thin films and their application for room temperature protein crystallography. *Sci. Rep.* **12**, 5349 (2022).

48. Singh, A. D. & Patrikar, R. M. Design and fabrication of PDMS-based electrostatically actuated MEMS cantilever beam. *Micro Nano Lett.* **15**, 302–307 (2020).

49. Conrad, H. et al. A small-gap electrostatic micro-actuator for large deflections. *Nat. Commun.* **6**, 10078 (2015).

50. Leroy, E., Hinchet, R. & Shea, H. Multimode hydraulically amplified electrostatic actuators for wearable haptics. *Adv. Mater.* **32**, 2002564 (2020).

51. Choi, C., Bansal, S., Münzenrieder, N. & Subramanian, S. Fabricating and assembling acoustic metamaterials and phononic crystals. *Adv. Eng. Mater.* **23**, 2000988 (2021).

52. Jiang, X., Li, Y. & Zhang, L. Thermoviscous effects on sound transmission through a metasurface of hybrid resonances. *J. Acoust. Soc. Am.* **141**, EL363–EL368 (2017).

53. Nyquist, H. Certain topics in telegraph transmission theory. *Trans. Am. Inst. Electr. Eng.* **47**, 617–644 (1928).

54. Marzo, A. et al. Holographic acoustic elements for manipulation of levitated objects. *Nat. Commun.* **6**, 8661 (2015).

55. Marzo, A. & Drinkwater, B. W. Holographic acoustic tweezers. *Proc. Natl. Acad. Sci. USA* **116**, 84–89 (2019).

56. Cao, H. X. et al. Holographic acoustic tweezers for 5-DoF manipulation of nanocarrier clusters toward targeted drug delivery. *Pharmaceutics* **14**, 1490 (2022).

57. Yuan, Z. et al. Ultrasonic tweezer for multifunctional droplet manipulation. *Sci. Adv.* **9**, eadg2352 (2023).

58. Ji, G. & Huber, J. Recent progress in acoustic metamaterials and active piezoelectric acoustic metamaterials - a review. *Appl. Mater. Today* **26**, 101260 (2022).

59. Noguchi, Y., Yamamoto, T., Matsushima, K. & Yamada, T. Labyrinthine acoustic metamaterials with a subwavelength bandgap inspired by topology-optimized structural design. *Adv. Eng. Mater.* **25**, 2201104 (2023).

60. Liu, T. W., Chan, C. T. & Wu, R. T. Deep-learning-based acoustic metamaterial design for attenuating structure-borne noise in auditory frequency bands. *Materials* **16**, 1879 (2023).

61. Lockette, Pvon et al. Investigating new symmetry classes in magnetorheological elastomers: cantilever bending behavior. *Smart Mater. Struct.* **20**, 105022 (2011).

62. Zhi, C., Shinshi, T., Saito, M. & Kato, K. Planar-type micro-electromagnetic actuators using patterned thin film permanent magnets and mesh type coils. *Sensors Actuators A Phys.* **220**, 365–372 (2014).

63. Vural, M. et al. Soft electromagnetic vibrotactile actuators with integrated vibration amplitude sensing. *ACS Appl. Mater. Interfaces* **15**, 30653–30622 (2023).

64. Ward, H. H. The seven-segment display and the stepper motor. In *Programming Arduino Projects with the PIC Microcontroller* (APress, Berkeley, CA 2022).

65. Venzac, B. et al. PDMS curing inhibition on 3D-printed molds: why? also, how to avoid it? *Anal. Chem.* **93**, 7180–7187 (2021).

66. Kwon, J. et al. Conductive ink with circular life cycle for printed electronics. *Adv. Mater.* **34**, 2202177 (2022).

67. Zhuang, Y. & Xie, R. Mechanoluminescence rebrightening the prospects of stress sensing: a review. *Adv. Mater.* **33**, 2005925 (2021).

68. Pagoli, A., Chapelle, F., Corrales-Ramon, J. A., Mezouar, Y. & Lapusta, Y. Review of soft fluidic actuators: classification and materials modeling analysis. *Smart Mater. Struct.* **31**, 013001 (2021).

69. Paternò, L. & Lorenzon, L. Soft robotics in wearable and implantable medical applications: translational challenges and future outlooks. *Front. Robot. AI* **10**, 7 (2023).

Acknowledgements

Author contributions

S.S., N.M., and C.C. conceived the project. Fabrication was led by C.C. with support from S.B., M.K.T., and N.M. Experiments, simulations, and data analysis were led by C.C., with contributions from all authors. S.B. and C.C. performed experimental measurements and data analysis. J.H. led the design and computation for the metasurface and assisted in the experimental design. C.C. wrote the paper, with contributions from all authors.

Competing interests

The authors declare no competing interests.

Additional information

Supplementary information The online version contains supplementary material available at https://doi.org/10.1038/s43246-023-00438-4.

Correspondence and requests for materials should be addressed to Christabel Choi.

Peer review information *Communications Materials* thanks Zhiwang Zhang and the other, anonymous, reviewer(s) for their contribution to the peer review of this work. Primary Handling Editors: Johan Christensen and Aldo Isidori. A peer review file is available.

Reprints and permission information is available at http://www.nature.com/reprints

Publisher's note Springer Nature remains neutral with regard to jurisdictional claims in published maps and institutional affiliations.